Deformation and phase transformation in polycrystalline cementite (Fe$_3$C) during single- and multi-pass sliding wear

Hanna Tsybenko [a],[*], Chunhua Tian [a], Julia Rau [b], Benjamin Breitbach [a], Paul Schreiber [b], Christian Greiner [b], Gerhard Dehm [a], Steffen Brinckmann [a],[c]

[a] Department Structure and Nano-/Micromechanics of Materials, Max-Planck-Institut für Eisenforschung GmbH, Düsseldorf, Germany
[b] MicroTribology Center μTC, Institute for Applied Materials (IAM), Karlsruhe Institute of Technology (KIT), Karlsruhe, Germany
[c] Forschungszentrum Jülich, Microstructure and Properties of Materials (IEK-2), Jülich, Germany

A B S T R A C T

Cementite (Fe$_3$C) plays a major role in the tribological performance of rail and bearing steels. Nonetheless, the current understanding of its deformation behavior during wear is limited because it is conventionally embedded in a matrix. Here, we investigate the deformation and chemical evolution of bulk polycrystalline cementite during single-pass sliding at a contact pressure of 31 GPa and reciprocating multi-pass sliding at 3.3 GPa. The deformation behavior of cementite was studied by electron backscatter diffraction for slip trace analysis and transmission electron microscopy. Our results demonstrate activation of several deformation mechanisms below the contact surface: dislocation slip, shear band formation, fragmentation, grain boundary sliding, and grain rotation. During sliding wear, cementite ductility is enhanced due to the confined volume, shear/compression domination, and potentially frictional heating. The microstructural alterations during multi-pass wear increase the subsurface nanoindentation hardness by up to 2.7 GPa. In addition, we report Hägg carbide (Fe$_5$C$_2$) formation in the uppermost deformed regions after both sliding experiments. Based on the results of electron and X-ray diffraction, as well as atom probe tomography, we propose potential sources of excess carbon and mechanisms that promote the phase transformation.

1. Introduction

Cementite is the Fe$_3$C-type iron carbide phase that affects the wear performance of bearing, rail, and wheel steels during rolling-sliding contact. While cementite is generally considered hard and brittle, it tends to exhibit plasticity in cases of specific microstructure morphologies and loading conditions [1,2]. In multiphase microstructures, such as pearlitic steels or martensitic bearing steels, the interactions between precipitates and matrix phase partially define the cementite deformation behavior [3–5]. Cyclic tribological loading causes continuous microstructural changes below the contact surface that, in return, constantly influence the frictional response [6]. As a consequence, when steel is exposed to the tribological load, there is a continuous interplay between altering cementite morphology, change of the dominant deformation mechanisms, and the effect cementite imposes on the overall wear performance.

Generally, cementite improves wear resistance by acting as a barrier to dislocation propagation and thus strengthens the steel. Pearlite has great strain-hardening potential through the mechanisms of stabilizing ferrite plasticity by elastically deformed cementite at early deformation stages [7,8] as well as microstructure refinement and interlamellar spacing reduction at later stages, i.e., Hall-Petch strengthening [1,9,10]. With a decrease of interlamellar spacing, pearlite gains a better wear performance [11], which leads to improved tribological stability compared to martensite, bainite, and ferrite with spheroidized cementite [12–15]. Pearlite and martensite deformation at high strains are often accompanied by the dissolution of cementite, which results in some degree of solid solution strengthening of the carbon-supersaturated ferrite [3,16–20].

Although cementite is an effective strengthening constituent in steels, two issues related to the drastic wear rate increase and material failure exist: precipitate cracking and microstructure transformation into brittle white etching layers/areas (WEL/WEA). Large spheroidized or grain boundary cementite inclusions are more difficult to deform plastically than thin lamellae, and therefore often

* Corresponding author.
E-mail address: h.tsybenko@mpie.de (H. Tsybenko).

act as crack nucleation sites [21–23]. Brittle fracture, in addition to dislocation slip of lamellar precipitates, was also observed in the cold-rolled steel [24]. The main argument for the preferred brittle fracture compared to dislocation-mediated plasticity in cementite is the insufficient number of independent slip planes for plasticity accommodation [25,26]. In rail and bearing steels exposed to cyclic rolling-sliding contact, the microstructure is initially responsible for strain hardening and improves the wear resistance; afterwards, the microstructure evolves into the brittle WEL/WEA. According to previous studies, microstructure evolution and cementite deformation are either partially responsible for the WEL/WEA formation in rails [27] or the main cause for this transformation [28]. More specifically, the WEL/WEA formation stages include severe plastic deformation and nanoscale refinement of the microstructure until complete cementite decomposition and incorporation of the released carbon into the Fe matrix [28]. These WEL/WEA regions and the associated fatigue cracks are responsible for rapid wear failures [27,29–31].

Based on the previous research, it is evident that cementite influences the tribological response of steel in many ways, both positively and negatively. Therefore, a better understanding of cementite deformation mechanisms during the early and late wear stages is needed for the ongoing development of wear-resistant steels. While many studies focus on the subsurface microstructure changes of rail, wheel, and bearing steels, the deformation behavior of cementite in these studies is largely controlled by the surrounding matrix phase and precipitate size. In the work of Umemoto et al. [5], the authors observed homogeneous lamella thinning by slip when the activated slip system in ferrite and the lamella plane are almost parallel. Inhomogeneous slip leads to the coarse slip step formation up to the fragmentation of lamellae into the 200–300 nm thick blocks that afterwards slide past one another. Karkina et al. [32] demonstrated that six slip systems of ferrite are available for the slip transfer across the ferrite-cementite interface. Zhang and Wang [33] analyzed martensitic bearing steel with embedded spheroidized cementite after mechanical rolling. Although direct slip transfer from the matrix into the precipitate was not observed, the inhomogeneous plastic flow of the surrounding martensite and the strain incompatibilities result in local stress concentrations. These stress concentrations allow for dislocation nucleation at these sites.

Production of bulk polycrystalline cementite by spark plasma sintering with and without the addition of stabilizing elements [34–36] allowed for the investigation of cementite wear behavior while excluding the contribution of the matrix. Sasaki et al. [37] compared the wear properties of specimens containing different fractions of cementite and single-phase cementite during pin abrasion experiments against alumina abrasive paper. The authors reported the wear performance for a range of applied pressures. On the one hand, ductile chip formation was detected in single-phase cementite at lower applied pressures (< 0.15 MPa). On the other hand, brittle cracking occurred, increasing wear weight loss at higher applied pressures (> 0.31 MPa) [37]. As a result, bulk cementite demonstrated the smallest wear volume loss among all studied compositions up to 0.61 MPa. At 1.23 MPa, the wear volume loss of bulk cementite was higher than that of the sample with 75% cementite [37]. A similar analysis of cementite volume fraction effect on the three-body wear behavior was conducted by Zheng et al. [35]. The sample was moved in a block-on-ring configuration against a steel countersurface covered with SiC particles at different applied pressures. At 0.098 MPa applied pressure, the authors report that fracture is the dominating wear mechanism of a single-phase cementite sample. The stronger abrasion leads to an increase of the wear weight loss of bulk cementite compared to the samples with smaller cementite fractions [35]. As such, the

present research on bulk cementite wear focuses on the effect of its fraction on wear resistance.

This work is an investigation of cementite deformation in a single phase under tribological loading. We study the microstructure evolution of sintered polycrystalline cementite by Umemoto et al. [34] in two loading cases: single-pass sliding at contact pressure of 31 GPa and multi-pass sliding at contact pressure of 3.3 GPa. To address cementite's limited ductility, we determine activated slip planes at the sides of the wear groove. By examining the deformed subsurface layers, we reveal that the dominating deformation mechanisms differ depending on the depth. The comparison between single-pass and multi-pass sliding allows us to understand the onset of microstructure alterations of cementite and how these initial deformation stages translate into the microstructure after cyclic loading.

Although this study focuses on the deformation behavior of cementite, the chemical evolution below the contact surface and the effect of tribological loading on the local strength are analyzed as well. We report on cementite transformation into an iron carbide, namely Hägg carbide Fe_5C_2, and propose mechanisms of its formation. In addition, we demonstrate how strengthening mechanisms during wear result in a significant hardness increase.

2. Experimental procedure

2.1. Material and sample preparation

High-purity Fe (99.9%) and C (99.9%) powders were mixed in a 3:1 ratio and mechanically alloyed for 20 h on a vibration ball mill in an argon atmosphere. After mechanical alloying, the powders underwent spark plasma sintering at 50 MPa at 900 °C for 15 min to produce bulk cementite samples (courtesy of Prof. Y. Todaka of the Toyohashi University of Technology). The cementite fabrication is described in detail in [34]. The as-received cementite was polished with 3 and 1 μm polycrystalline diamond suspension (Struers) and the colloidal silicon oxide polishing suspension (OPS, Struers) to reach a smooth and flat surface. The average surface roughness was ~10 nm, as determined by the topography line scan at 0.15 mN force before the single-pass scratch experiment [38].

The phases of the cementite sample and the initial grain size were characterized using X-ray diffraction (XRD). Cementite is present in 94.5 vol.% of the sample volume with an average grain size of 436 ± 18 nm. Small fractions of iron (2.9 vol.%) and iron oxide FeO (2.6 vol.%) were detected as well. We also observed in the scanning electron microscope (SEM) images (Section 3.1.1), transmission electron microscope (TEM) images and diffraction patterns, as well as energy-dispersive X-ray spectroscopy measurements (EDS, Figs. A1–A3 in Appendix A) some graphite that did not transform during sintering. In the original work by Umemoto et al. [34], a relative sample density of 98% was reported. Hence, some porosity is present in the sample.

2.2. Wear experiments

We conducted a single-pass microscale wear experiment in a KLA (Agilent, Keysight) G200 Nanoindenter with a sphero-conical diamond tip (Synton-MDP) with a 5 μm radius. The experiment starts with the tip indenting the sample until a specified normal load is reached. Then the sample is moved laterally with constant velocity and normal load [39,40]. We employed 10 μm/s velocity and 100 mN normal load, which leads to a reference Hertzian pressure [41] of 31 GPa. In the evaluation of the Hertzian pressure, we used Young's moduli and Poisson ratios of 1141 GPa and 0.07 for the diamond tip, as well as 204 GPa and 0.36 for cementite. The normal load was selected to ensure severe deformation inside the wear track. Using the scratch hardness of cementite H_S = 14.8 GPa

[38] and assuming a half-circular contact area during wear, we determine contact depth as 0.45 μm.

For the multi-pass wear experiment, a linear reciprocating tribometer was employed [42]. A sapphire sphere (Saphirwerk) with a diameter of 10 mm was reciprocally moved on the sample surface at a frequency of 25 Hz and a normal load of 230 N. The contact depth for a single stroke was calculated as 0.99 μm. The reference Hertzian contact pressure was calculated as 3.3 GPa. We used for the sapphire a Young's modulus of 345 GPa and a Poisson ratio of 0.3. The pressure was nearly 10 times smaller than the contact pressure for the single-pass wear experiment. With a stroke distance of 5 mm, 2000 strokes were performed – resulting in an overall sliding distance of 10 m.

To examine the effect of cyclic wear on hardness, we carried out nanoindentation tests on undeformed cementite and smooth non-fractured surface regions after the multi-pass experiment. Nanoindentation was performed in the G200 Nanoindenter using a Berkovich tip and the continuous stiffness measurement technique at a constant strain rate of 0.05 s^{-1}. The target depth was 1.2 μm.

2.3. Microstructure and composition characterization

The worn surfaces were imaged in a Zeiss Gemini SEM with a secondary electron detector. For the slip trace analysis, we conducted electron backscatter diffraction (EBSD) measurement on the side of the single-pass wear track groove using an EDAX detector in a Zeiss Auriga focused ion beam (FIB) SEM workstation. The scan step was 20 nm. Crystallographic orientation was studied in the TSL OIM 7 software.

The initial quantitative XRD phase analysis was carried out in Bragg-Brentano geometry using a Bruker D8 Advance A25-X1 diffractometer with Co-Kα X-ray source ($\lambda = 1.79$ Å) and LYNX-EYE XE-T energy-dispersive 1D detector. For the measurements on the worn surface after the multi-pass wear experiment, a Rigaku SmartLab 9KW diffractometer with Cu-Kα ($\lambda = 1.54$ Å) radiation was employed. The measurement was conducted in the parallel beam geometry, with the micro-area CBOμ optics setup (125 μm beam) and HyPix 3000 2D detector. The theoretical penetration depth for XRD was calculated with the AbsorbX software using the cementite density 7.69 g/cm³ and the Cu-Kα radiation source.

Specimens for TEM and scanning transmission electron microscopy (STEM) were prepared using a lift-out technique in a Thermo Fisher Scientific Scios 2 DualBeam FIB-SEM system with Ga$^+$ ion source at 30 kV acceleration voltage. The beam current varied from 1.6 nA during coarse milling to 10 pA at the final polishing and cleaning steps at a specimen thickness of about 100 nm. TEM, STEM as well as EDS (see Appendix A) studies were conducted in JEOL JEM-2200FS, and JEOL JEM 2100PLUS microscopes operated at 200 kV acceleration voltage.

For the elemental distribution measurements in the topmost deformed region after the single-pass wear experiment, we performed atom probe tomography (APT). The needle-like tips were milled using FEI Helios NanoLab 600 Dual Beam FIB/SEM with Ga$^+$ ion source at 30 kV. The current changed from 9 nA for coarse milling to 0.23 nA, 80 pA, and 24 pA for sharpening the tip to the diameter of about 80 nm. The final cleaning step was executed at 5 kV and 15 pA. The APT measurements were carried out in a Cameca LEAP 5000XR atom probe instrument in voltage mode (15% pulse fraction, 200 kHz pulse frequency) with a 0.5% detection rate and at a temperature of 60 K. We used a software package AP Suite 6.1 for data analysis and tip reconstruction.

The overestimation of carbon in iron carbides during APT measurements is often observed in literature and is explained by the effect of specimen temperature on iron ion detection [43,44]. At specimen temperatures below 60 K, the multiple-hit events and ion pile-up induce the detection loss of iron. The deviation from

the expected carbon content is more substantial for the pulsed voltage atom probe than the pulsed laser atom probe [45]. The difficulty in determining the absolute carbon content also arises from the mass-to-charge 24 Da carbon peak assignment, which can be either C_2^+ or C_4^{2+} or a mixture of both [46]. We consistently distribute the peak 24 Da to half C_2^+ and half C_4^{2+}. The other peaks 6 and 6.5, 12 and 13, 18 and 18.5, 24.5 and 36 Da are assigned without ambiguity to C^{2+}, C^+, C_3^{2+}, C_4^{2+} and C_3^+, respectively. Another source for carbon overestimation is related to the crystallographic poles that affect the field evaporation [47] and result in the straight columnar structures on tip reconstructions. These structures are considered measurement artifacts. The 1D profile and area fraction measurements were performed outside the crystallographic pole artifacts.

3. Results and interpretation

3.1. Single-pass wear

3.1.1. Microstructure evolution and deformation mechanisms

As mentioned in Section 2.1, the microstructure of the sintered sample consists primarily of fine-grained cementite (Fig. 1a). The remaining iron, iron oxide, and graphite are distributed differently. Iron is mainly present as grains of similar size as cementite. Some iron also formed finely dispersed iron oxide (white ultrafine particles on Fig. 1a). Graphite is partially stored in the elongated plate-like inclusions and is also present as spherical particles (appear black on Fig. 1a) of the same size as iron oxides. Both iron oxide and graphite are found at cementite grain boundaries, while some are located inside cementite grains. The initial composition of the non-cementite phases was examined by EDS (Fig. A1, Appendix A). The diffraction pattern obtained from the carbon-rich particle demonstrates graphite reflections (Fig. A2 in Appendix A).The undeformed cementite grains contain few dislocations (Fig. A3 in Appendix A).

We start by inspecting the cementite surface after the single-pass wear experiment at high contact pressure (31 GPa, Fig. 1b). In the indentation region "I" of the wear track (marked by a white bracket on Fig. 1b), we observe distinct slip traces and deformed graphite particles. After the transition to plastic plowing, the wear groove appears relatively smooth, homogeneous, and non-cementite inclusions are barely visible. Slip traces and wear debris are also found at the wear track edge. The front pile-up consists of moderately ductile flakes. The observed wear features thus are more typical for plastically deforming materials. Only a single crack was found at the groove edge near the indentation region. Therefore, the dominating wear mechanisms are plastic plowing and microcutting, and the plastic deformation below the contact surface is mainly due to extensive compression and shear strains.

To investigate the activated slip planes in orthorhombic cementite during wear, we analyzed slip traces in the grains on the wear track edges (Fig. 2). To this end, SEM images and EBSD orientation maps of the same wear track region were studied. For the measured crystallographic orientation of each studied grain, possible slip planes were plotted. Afterwards, the experimentally observed slip traces were superimposed with the pole figures to determine the activated slip planes.

Among 10 studied grains at the wear track edge, (001), (010), (101), (110), and (011) slip planes were identified. The (001), (010), and (011) planes were activated in two grains each. In three grains, activated (101) planes were indexed, and in one case, slip on both (110) and (101) planes was observed. These findings are in good agreement with the previously reported slip planes of cementite: the predominantly but not uniquely found slip planes at ambient temperature deformation of cementite are (001), (010), and (100) [48,49]. Other (101), (110), and (011) planes usually become avail-
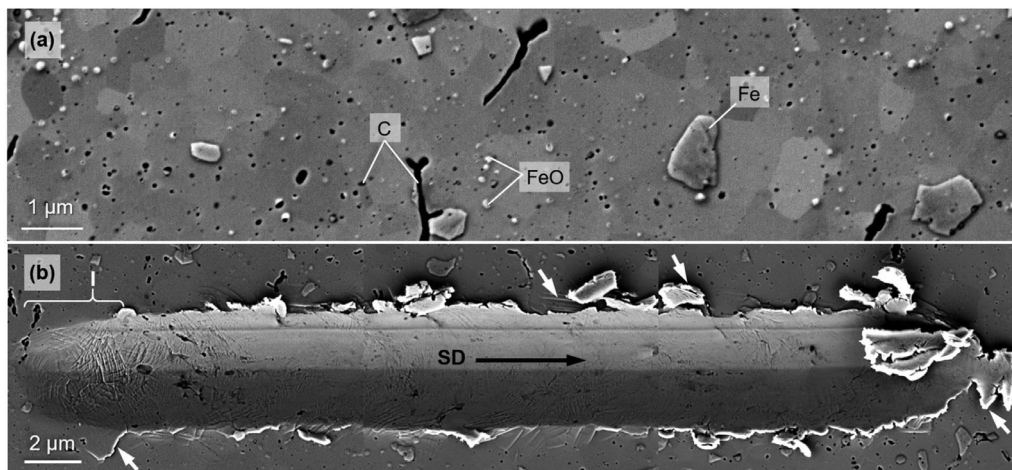
Fig. 1. SEM images of the cementite surface (a) before and (b) after the single-pass wear experiment. (a) Initial sample microstructure with iron, iron oxide, and graphite inclusions that remain after spark plasma sintering. (b) Combined (of three images at the different wear track regions) image of the single-pass wear track with a black arrow showing the sliding direction (SD). White arrows mark wear features: a single crack event, plastic slip traces, wear debris, and pile-up at the wear track end. The white bracket denotes the indentation region "I".
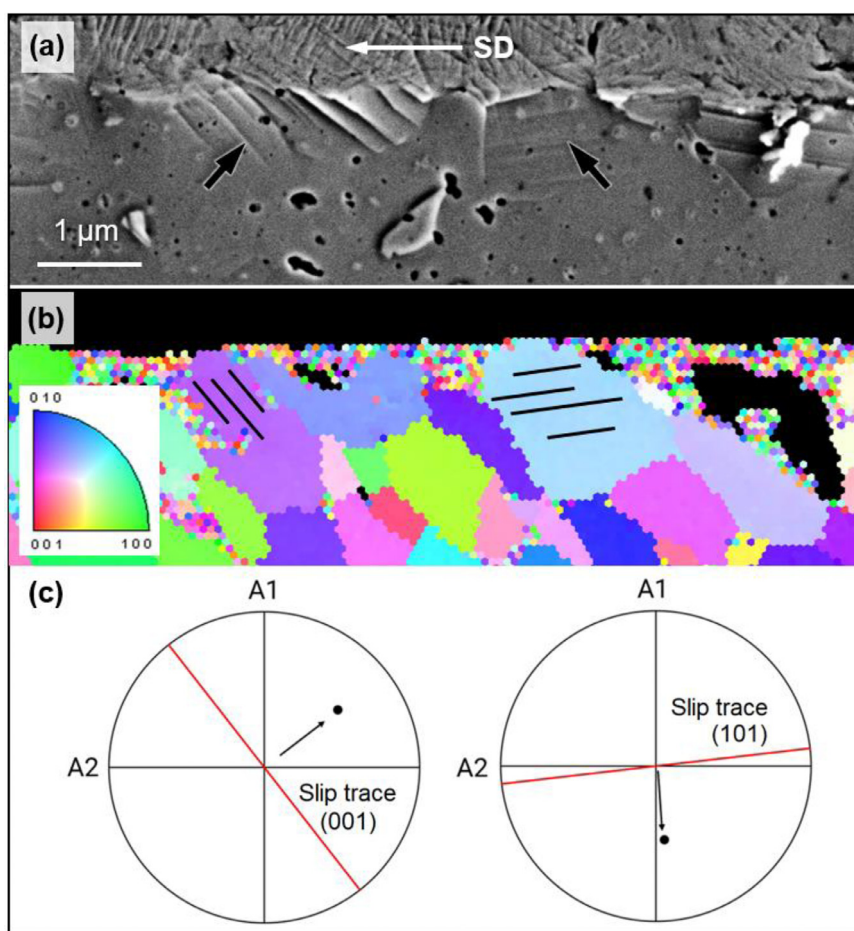

Fig. 2. An example of the slip trace analysis. (a) SEM image of the wear track edge, showing slip traces in several cementite grains. The analyzed slip traces are marked with black arrows. The white arrow denotes a sliding direction (SD). (b) EBSD orientation map with superimposed slip traces of two studied grains (black lines). (c) Constructed pole figures based on the EBSD orientation (purple and light blue in b). The black dot is the pole of identified slip plane. The red line represents the intersection of the slip plane with the top surface (the slip trace), which corresponds well with the traces from SEM images in (a). (For interpretation of the references to color in this figure legend, the reader is referred to the web version of this article.)
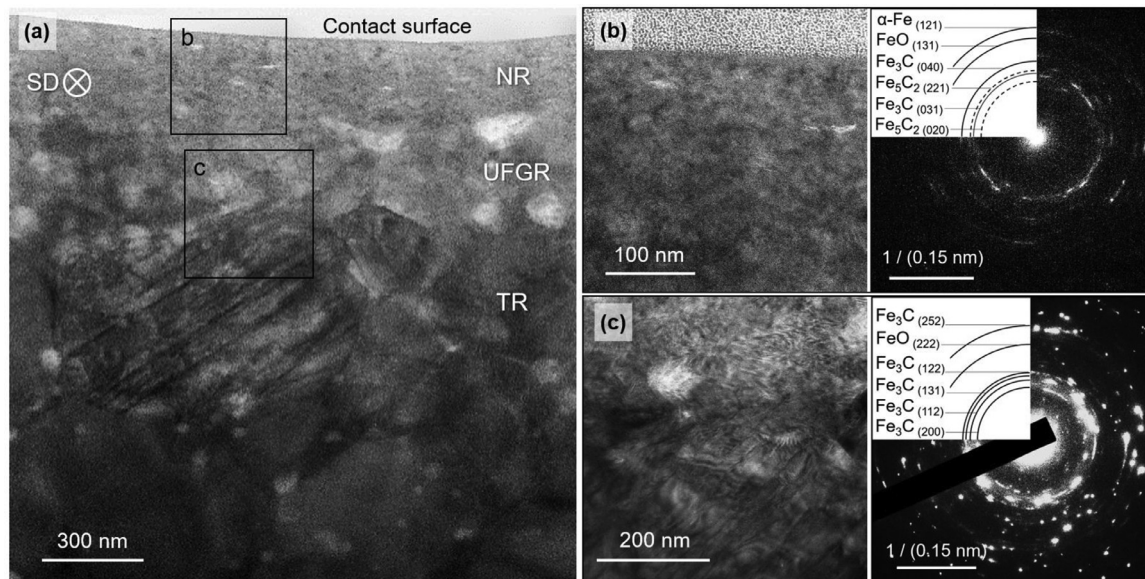
Fig. 3. TEM and STEM overview micrographs of the wear track cross-section after a single-pass experiment. SD marks the sliding direction. (a) STEM bright-field (BF) image of the wear track cross-section with marked characteristic deformed regions. (b) TEM image of the nanocrystalline region (NR) with corresponding diffraction pattern. (c) TEM image of the area with the ultra-fine-grained region (UFGR), transition region (TR), and corresponding diffraction pattern.

able for dislocation glide at high temperature [48], for the lamellar morphology [50], or under high rolling strains [33,51].

In order to examine the microstructure evolution, we studied a wear track cross-section in TEM. Fig. 3a demonstrates the plastically deformed region with about 1.5 μm thickness which has a layered structure. Below the deformed regions, pristine cementite grains (dark gray), as well as finely dispersed undeformed iron oxide and graphite inclusions (light gray on Fig. 3a) are observed.

Overall, three distinct deformation zones are resolved (Fig. 3a): a nanocrystalline region just below the wear track, followed by an ultra-fine-grained region, and transition region until the undeformed bulk cementite is reached at a depth of ca. 1.5 μm. In the uppermost 200–300 nm thick nanocrystalline region, the highest shear strains and strain rates promoted grain refinement inducing an average grain size as low as ∼10 nm. Most of the non-cementite particles (iron oxide and graphite) were heavily deformed and are not discernible. Therefore, the resulting nanograin structure is relatively homogeneous. The nanocrystalline region is separated from the lower ultra-fine-grained region by a relatively abrupt transition. The 250 nm thick ultra-fine-grained region possesses a grain size of 100–200 nm. Cementite is severely fragmented and plastically deformed. The iron oxide and graphite particles are deformed as well but remain similar in size as for the undeformed bulk material. The lowest deformation layer is the transition region with a thickness of ∼1 μm. The cementite grains in the transition region reveal dislocation slip but are not fragmented into fine blocks, as they are in the ultra-fine-grained region.

For an overview, two diffraction patterns were obtained from the nanocrystalline region and the intersection of the ultra-fine-grained and transition regions. The diffraction pattern from the nanocrystalline region consists of multiple discontinuous rings (Fig. 3b) due to the nanoscale grain refinement and evolving texture. Although most reflections are assigned to cementite, iron, or iron oxide, some diffraction arcs correspond to the Hägg carbide Fe_5C_2. This phase was examined more closely in the following section. Some of the reflections would match as well to the ε-carbide phase Fe_2C. However, since no unique ε-carbide reflection (i.e., not overlapping with any of the other phases) was found, the possibility of ε-carbide formation is not discussed further.

Another diffraction pattern was obtained from both the transition and ultra-fine-grained regions (Fig. 3c). The reflections are primarily individual spots, but arcs due to the high density of dislocations are also observed. A diffuse halo in the area of the strongest reflections is due to graphite particles. We indexed the diffraction spots mainly as cementite and iron oxide, and none of the spots was assigned to Hägg carbide.

We characterize the transition region in more detail to explain the mechanisms of cementite refinement under tribological load (Fig. 4a). In the transition region, plasticity is predominantly accommodated by dislocation slip. High local stress concentrations cause the gliding of large amounts of dislocations on relatively few, often well separated, parallel slip planes (Fig. 4b). Dislocations thus form coarse slip steps with a height up to 40 nm (marked by the black bracket on Fig. 4b) and cut through the non-cementite particles. In Fig. 4c, we observe slip transfer across the grain boundary while some residual dislocations are piling up. In some cases, deformation transfer between neighboring grains is accompanied by the locally intensified shear, which is accommodated by shear bands (Fig. 4d). In summary, cementite deformation in the transition region is inhomogeneous and results in grain fragmentation. Fig. 4e shows an onset of the fine cementite fragment formation (approximate dimensions 110 × 120 nm) by slip on the intersecting slip planes.

3.1.2. Hägg carbide formation

To further investigate the formation of Hägg carbide, we recorded another diffraction pattern by placing the selected area aperture in the middle of the nanocrystalline region (Fig. 5a,b). The majority of spots and rings were assigned to Hägg carbide, while some cementite and iron oxide reflections were also found. The objective aperture was then placed on two selected Hägg carbide reflections (221) and (112) (marked by red circles on Fig. 5c,d) to record the dark-field images produced by the diffracted beams. The resulting micrographs (Fig. 5c,d) demonstrate that nanometer-sized Hägg carbide crystallites are homogeneously distributed solely inside the nanocrystalline region and not in the ultra-fine-grained region. Most of these carbides are present in the middle of the nanocrystalline layer. This observation indicates that sufficiently
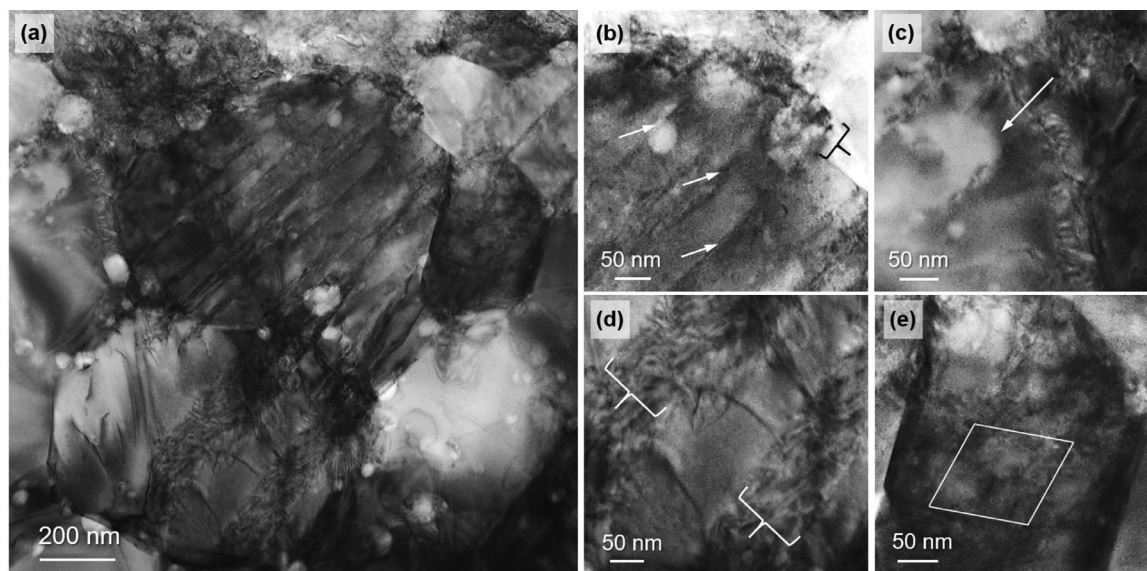
Fig. 4. (a) STEM BF micrograph of the transition region demonstrating plastic deformation of polycrystalline cementite. (b) Coarse slip steps (as highlighted with a bracket) are produced by the large number of dislocations passing on slip planes (marked with white arrows). (c) Slip transfer through the grain boundary (white arrow denotes the direction) and dislocation accumulation. (d) Shear bands (marked by brackets) and pinned dislocations between them. (e) Grain fragmentation into fine blocks by multiple slip events (a single block marked with white lines).

high shear strains and nanoscale refinement are required to induce the phase transformation.

We conducted APT measurements in the undeformed cementite grain and the nanocrystalline region below the contact surface to study the local carbon distribution. Tip reconstructions with different carbon isosurfaces as well as 1D carbon and iron content profiles are given in Fig. A4 (Appendix A). Fig. 6 shows the needle reconstructions with 33 at.% C and 0.3 at.% O isosurfaces. While the exact absolute carbon contents are difficult to achieve due to several sources for carbon overestimation in APT (Section 2.3), a relative comparison of the composition is possible.

Based on the 1D profiles (Fig. A4c,d in Appendix A), the average carbon content and the C/Fe ratios in the undeformed grain and nanocrystalline region are comparable. However, the carbon content increases locally in the deformed region (Fig. 6). The fraction of 33 at.% C isosurface area estimated in magnified insets in Fig. 6 is considerably higher in the nanocrystalline region ($\sim$13%) when compared to the undeformed cementite ($\sim$7%). In addition, the oxygen content is also higher in the nanocrystalline region, as more 0.3 at.% O isosurfaces are visible in Fig. 6b ($\sim$17% area in the nanocrystalline region versus $\sim$11% area in undeformed grain). A slight increase in the average oxygen content is also evident from the 1D profiles (Appendix A).

3.2. Multi-pass wear

3.2.1. Microstructure evolution and deformation mechanisms

The multi-pass wear experiment with the contact pressure of 3.3 GPa was carried out to compare the microstructure evolution with the single-pass experiment at the contact pressure of 31 GPa. Fig. 7a demonstrates the heavily deformed worn surface with a large amount of wear debris. The tribolayer (darker area in Fig. 7b) is mainly composed of the material transferred from the sapphire tip and some iron oxide. Even on the much softer copper oxide, aluminum on the worn surface was also found after multi-pass wear with the sapphire tip [52]. The abraded particles from the removed tribolayer and repeated sliding lead to the contact fatigue, which results in the nucleation of brittle cracks at the surface (Fig. 7b). As a result, the loose wear debris is composed of the removed tribolayer and fractured cementite, promoting three-body

abrasive wear. Outside the fractured regions, the deformed cementite surface is similar to the steady-state region of the single-pass wear track, which indicates nanocrystal formation (Fig. 1b). While no slip traces are observed, shallow plowing marks are visible. Other surfaces appear relatively smooth compared to the fractured regions. The non-cementite particles are not distinguishable.

We characterize the multi-pass wear track cross-section (outside the fractured areas) in TEM. The overall thickness of the plastically deformed cementite is much larger than for the single-pass scratch and extends over the entire length of the TEM specimen (Fig. 8a). The three previously defined regions during single-pass wear are observed in the case of multi-pass wear as well. However, we find a number of distinctions between the microstructures after the two different loading conditions.

The nanocrystalline region (Fig. 8b) in the multi-pass case is similarly thick (200 nm) compared to the single-pass wear track (Fig. 3a). It is noteworthy that non-cementite particles are highly deformed, partially decomposed but still visible in some areas near the surface while absent further below the surface. The nanocrystalline region has an average grain size of about 20 nm and is gradually transitioning into the ultra-fine-grained region, as no sharp interface between the two regions is identifiable. The ultra-fine-grained region covers most of the specimen height (4 μm). Iron oxide and graphite particles are mostly deformed and elongated in the direction of the highest in-plane shear stress. These elongated inclusions are likely the sites for crack initiation during contact fatigue (Fig. 7b). Some larger graphite particles are found as well. In the transition region, the grains are not distinctively fragmented by slip on a small number of parallel far-spaced slip planes, as in the single-pass case. Coarse slip steps and shear bands are not observed, and the non-cementite particles appear undeformed. Nonetheless, the density of homogeneously distributed dislocation lines and dislocation loops is high.

3.2.2. Effect of multi-pass wear on the near-surface strengthening and Hägg carbide formation

The strengthening effect on the surface hardness was studied by nanoindentation. Fig. 9a compares hardness as a function of the penetration depth until 1200 nm for the undeformed area as well as the smooth non-fractured area of the worn surface. The average
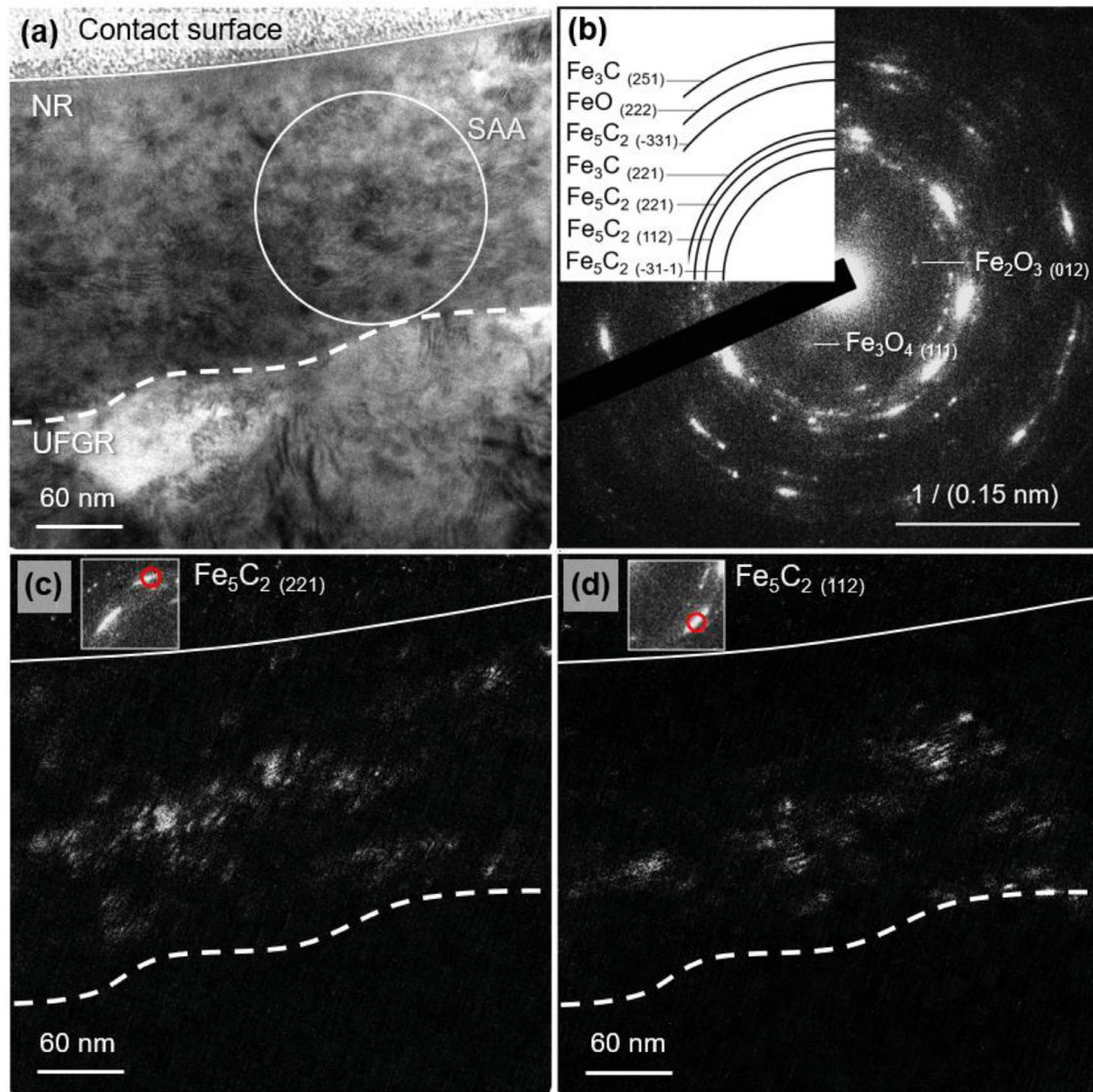
Fig. 5. Hägg carbide formation below contact surface. A dashed line marks the interface between the nanocrystalline region (NR) and the ultra-fine-grained region (UFGR), and a thin solid line defines the surface. (a) TEM image of the nanocrystalline and ultra-fine-grained regions and the position of the selected area aperture (white circle). (b) Diffraction pattern recorded from the nanocrystalline region demonstrating cementite, iron oxide, and Hägg carbide reflections. (c), (d) Dark-field images from the selected Hägg carbide reflections. Red circles in the inserted diffraction pattern fragments mark the positions of the objective aperture used to obtain the respective images.

hardness at 500 nm ($H_{500\ nm}$) was calculated using a depth range of 400–600 nm, whereas the 1000 nm hardness ($H_{1000\ nm}$) was determined by averaging the values between 900 and 1100 nm. The scatter is slightly higher in the deformed case but remains comparable to the undeformed curves. The hardness increase $\Delta H_{500\ nm}$ and $\Delta H_{1000\ nm}$ of the worn area compared to the undeformed sample are 2.7 GPa and 2 GPa, respectively. Hence, we demonstrate a strong local increase of hardness due to strain hardening after severe deformation of cementite during tribological loading

The XRD measurements were conducted to analyze the relation between microstructure refinement and phase transformation. The calculated X-ray penetration depth in cementite (Section 2.3) varies from 0.9 μm (at $2\theta = 20°$) to 4.6 μm ($2\theta = 120°$). In the region of the major reflections ($2\theta \sim 45°$), the penetration depth was 2.05 μm.

As shown in Fig. 9b for an undeformed area, cementite reflections are strong; whereas, in the worn region, the intensity decreases and peaks broaden due to grain refinement and a high dislocation density. In the deformed case, cementite peaks appear to shift to lower angles, attributed to lattice distortion and increased interplanar spacing as strain increases. Some reflections weaken in the worn case compared to the undeformed sample, while the intensity of others remains roughly similar. For instance, the strongest cementite (031) reflection ($2\theta = 44.9°$) loses most of its intensity, whereas the (220) peak ($2\theta = 44.6°$) remains relatively strong. These observations indicate texture development. According to the results of the Rietveld analysis [53], the average crystallite size decreased from 436 ± 18 nm in the undeformed area to 9 ± 1 nm after cyclic tribological loading.

In Section 3.1.2, we relate the nanoscale grain refinement below the contact surface to the formation of Hägg carbide. When comparing experimental XRD patterns with the superimposed peak position lines, we do not identify any Hägg carbide reflections. The intensity at the major Hägg carbide reflections ($2\theta = 43.5, 44°$) slightly increases because of the cementite peak broadening and overlapping. This observation is consistent with our findings that demonstrate the formation of Hägg carbide in the nanocrystalline region but not in the ultra-fine-grained region (Fig. 5). Since the
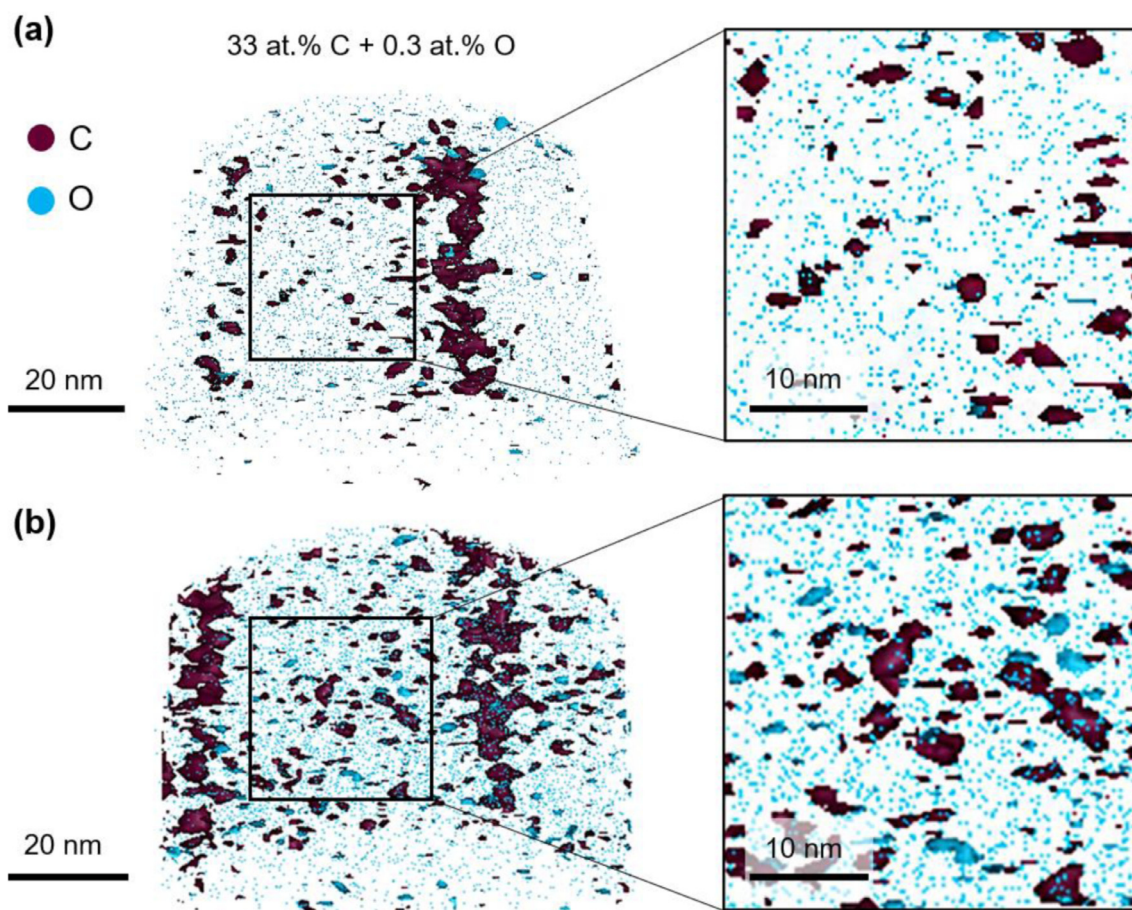
Fig. 6. 3D reconstructions of the APT specimens showing 33 at.% C and 0.3 at.% O isosurfaces. Columnar structures correspond to the crystallographic poles. The insets of higher magnification demonstrate the regions where carbon and oxygen isosurface area fractions were quantified. (a) Undeformed cementite grain. (b) Nanocrystalline region below the contact surface.
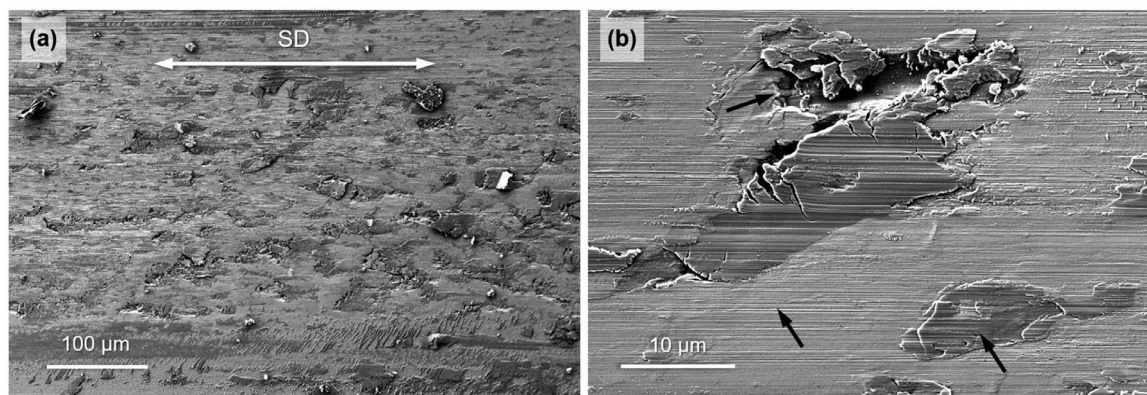

Fig. 7. SEM images of the cementite surface after the multi-pass sliding wear. (a) Overview of the worn surface. The white arrow shows the direction of the reciprocating sliding motion (SD). (b) Wear features after the multi-pass wear experiment (marked with black arrows): plowing marks, material transfer, and fractured cementite.

penetration depth during XRD was 0.9–4.6 μm, a large portion of the XRD data stems from outside the 200 nm thick nanocrystalline region.

While inspecting the electron diffraction pattern from the nanocrystalline region and the ultra-fine-grain region of the multi-pass wear track, we observe rings attributed to Hägg carbides (Fig. 10). These findings are similar to those of the single-pass experiment. Other reflections are indexed as cementite and iron oxides.

4. Discussion

4.1. Deformability of cementite during tribological loading

The deformability of cementite is generally a point of interest. The number of independent slip systems is assumed to be limited, and cross-slip is hindered. Hence, cementite is considered inherently brittle [25,50,54]. At high temperatures, activation of specific dislocation glide systems is reported in the literature
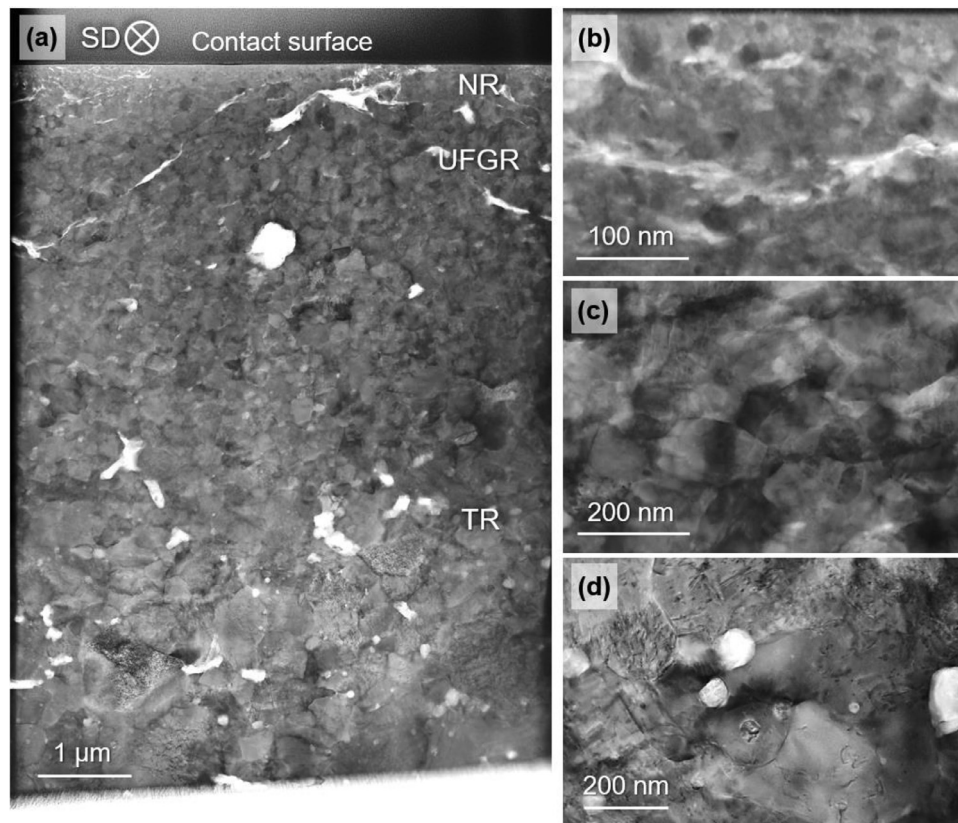
Fig. 8. STEM BF micrographs of the wear track cross-section after the multi-pass experiment with marked deformed regions. SD marks the sliding direction. (a) Overview of the deformed regions. (b) Nanocrystalline region (NR). (c) Ultra-fine-grained region (UFGR). (d) Transition region (TR).
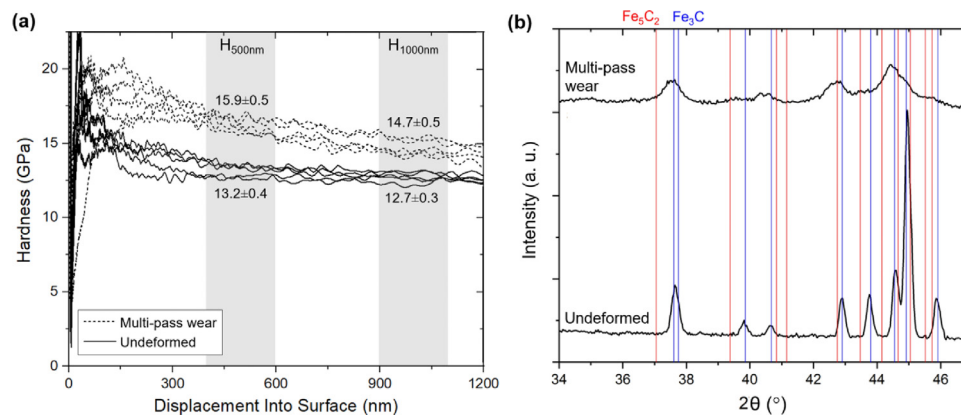

Fig. 9. (a) Nanoindentation hardness measured on undeformed (solid lines) and worn cementite (dashed lines). The gray areas mark the depth ranges where the average hardness values were determined. (b) XRD patterns obtained from the undeformed cementite and inside the multi-pass wear track with superimposed peak positions of cementite (blue lines) and Hägg carbide (red lines). The 2θ range was selected to show the strongest experimental reflections. (For interpretation of the references to color in this figure legend, the reader is referred to the web version of this article.)

[48]. Dislocation plasticity under specific loading conditions is reported [33,50,51]. In our study, cementite tends to deform plastically through the activation of multiple slip systems during sliding wear (Fig. 2). Below the contact surface (Figs. 3, 8), plastic deformation is accommodated by several mechanisms discussed in the following section.

The increased cementite ductility is promoted by the relatively constrained volume during tribological loading. In this regard, sliding wear is similar to the other severe plastic deformation techniques, where the constrained specimen volume during processing causes a substantial increase in hydrostatic pressure, affecting the deformation behavior of the material [55,56]. During deforma-

tion under high hydrostatic pressure conditions, e.g., high pressure torsion, cementite shows notable plasticity when embedded in a matrix [3,57]. In our case, wear experiments on the polycrystalline bulk cementite also result in a local increase of hydrostatic pressure and, thus, ductility enhancement.

Another crucial factor for cementite deformability is the dynamically evolving stress-strain field as the tip is plowing through the material during sliding contact. Based on the single-asperity sliding model by Hamilton [58], the compressive stresses increase in front of the passing tip, while tensile stresses grow at the tip backside in the plane of the normal and sliding directions. Shear stresses intensify below the contact surface, whereas the exact po-
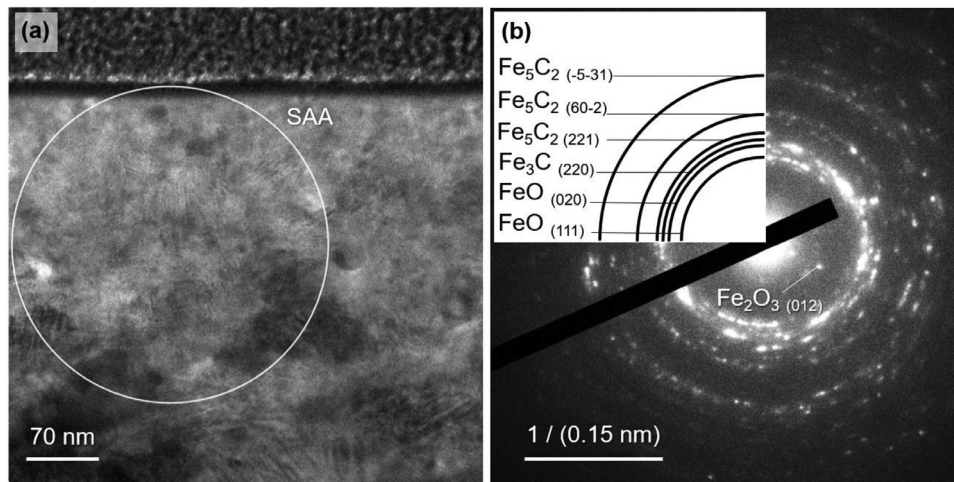
Fig. 10. (a) Nanocrystalline region transitioning into the ultra-fine-grained region below the contact surface of the multi-pass wear track with a marked position of the selected area aperture (SAA) and (b) corresponding diffraction pattern with reflections mainly assigned to cementite, iron oxides, and Hägg carbide.

sition of the maximum normalized von Mises yield parameter depends on the friction coefficient [58]. Therefore, the deformation below the contact surface (Figs. 3, 8) primarily results from the high compressive and shear stresses.

During sliding wear, frictional heat can lead to temperature increase that can further promote cementite ductility. Several studies pointed out the drastic increase of temperature in the rail-wheel contact zone [59,60]. In the single-pass wear experiment, the wear velocity is relatively low, the local temperature rise is a rapid one-time event, and frictional heat immediately dissipates. However, for multi-pass wear track, due to a large number of strokes and a high sliding frequency of 25 Hz, frictional heat in the contact zone potentially affects cementite deformability. Nonetheless, the relative contributions of frictional heat as well as other factors that affect the ductility of cementite require further discussion and are not central to this study.

4.2. Microstructure evolution below the contact surface

In this section, we describe the microstructure evolution of bulk polycrystalline cementite during tribological loading. Since the compression and shear stresses gradually decrease with the increasing depth, gradient microstructures are formed in both single-pass and multi-pass experiments. By analyzing the microstructures after both experiments, we define cementite deformation mechanisms depending on the loading conditions.

4.2.1. Single-pass wear

In the transition region, cementite grains deform predominantly through dislocation glide (Fig. 4). Although the overall stresses are lower in the transition region than directly below the contact surface, the local stress concentrations cause a high dislocation activity on far-spaced slip planes. The separation of activated slip planes may be a consequence of the limited number of dislocation sources inside the cementite grains, as the undeformed cementite reveals very few dislocations (Fig. A3 in Appendix A). As a result, the deformation is highly inhomogeneous and causes the formation of coarse slip steps (Fig. 4b), and subsequently, grain fragmentation (Fig. 4e). The fragmentation of the original spheroidized cementite grains into the fine blocks by slip was previously reported during dry sliding of steels [3,33]. In those works, the stress intensifies at the matrix-cementite interface due to the matrix flow around the cementite particles until the cementite shear strength

is reached. In the case of the polycrystalline cementite, the load is transferred from the shallow, highly deformed ultra-fine-grained layer and within the transition region during sliding wear. Inhomogeneous slip in the highly deformed grains results in dislocations pile-up and stress concentrations at the grain boundaries (Fig. 4c). When the transferred shear strain is sufficiently intense, shear bands form (Fig. 4d).

In the ultra-fine-grained region, moderate shear stresses result in the complete fragmentation of the initial cementite grains into 100–200 nm subgrains (Fig. 3a). Further shearing by dislocation slip is less pronounced at this grain size, and we propose that grain boundary sliding is the dominant deformation mechanism. This change of favored deformation mechanism at different grain sizes is consistent with molecular dynamics simulations of polycrystalline cementite subjected to tensile loading by Ghaffarian et al. [26]. As the grain size decreases, dislocation glide becomes less preferred, and grain boundary sliding accommodates plasticity instead [26]. In the work of Terashima et al. [2], bulk polycrystalline cementite with the average grain size of 0.7 μm exhibited brittle failure during room temperature compression, whereas at elevated temperatures, extensive ductility through grain boundary sliding was achieved. On the other hand, Todaka et al. [24] reported sliding of 100–200 nm cementite fragments as one of the main cementite deformation mechanisms in pearlitic steel during cold rolling. Although the matrix influences cementite deformation mechanisms in pearlitic steels, the reported findings agree with our observations: a sufficiently small grain size is required for cementite to deform by grain boundary sliding at room temperature. These small grains develop by fragmentation of the initially larger grains.

In the nanocrystalline region (Fig. 3b), severe deformation facilitates the further reduction of the grain size to the nanoscale. Below the contact surface, the highest shear stresses result in the accommodation of the highest strains compared to the other subsurface depths. These intense localized strains result in further grain refinement potentially through a mechanism similar to shear band formation. The refined nanoscale subgrains deform by grain boundary sliding and grain rotation, similarly to the nanostructured cementite crystallites in highly strained cold-drawn pearlite wires [61]. Since carbon tends to reduce the saturation grain size during severe plastic deformation by suppressing grain boundary sliding [62], the mechanically mixed carbon from decomposed graphite inclusions likely affects the grain size in the nanocrystalline region.

4.2.2. Multi-pass wear

We now discuss the microstructure alterations during multi-pass wear while considering the unraveled deformation mechanisms during single-pass wear. It is noteworthy that these wear experiments are substantially different. Regarding the loading conditions, the single-pass wear track was conducted at high contact pressure but low wear velocity, as opposed to the multi-pass test, in which moderate contact pressures and a high wear velocity were employed.

The principal difference between both experiments is the number of wear passes and the sliding direction. We executed the single-pass test as a single asperity unidirectional sliding contact. Hence, there is an analogy to the contact model of Hamilton [58]. However, the multi-pass wear track was produced by cyclic reciprocating sliding with a large counterbody, resulting in multiple asperity contact. The friction coefficient and the corresponding material response below the contact surface differ from the single-pass wear and change with each tip stroke. The material transfer from the tip to the contact surface affects the wear response as well. Moreover, contact fatigue is accompanied by abrasive debris formation (Fig. 7), leading to the three-body contact regime. Therefore, during multi-pass wear, the stress-strain state below the contact surface and the microstructure evolution are dynamically evolving and much more complex than the single-pass experiment. Overall, the single-pass wear experiment provides better insight into the cementite deformation mechanisms based on the loading state, whereas the multi-pass experiment resembles microstructure evolution in real contact.

Despite the differences in loading conditions, wear directions, and tip-materials, the comparison of the subsurface microstructures after both sliding tests reveals the same deformation mechanisms that accommodate plasticity. However, their relative contributions to the microstructure alterations are different. In the multipass experiment, the transition region is located further from the contact surface, compared to the single-pass case. As the transition region is located lower and the applied load is lower than for the single-pass wear, the stress intensities are generally lower, and the stress field is more homogeneous than in the transition region of the single-pass wear track. Consequently, the dislocation activity is more homogeneous, the slip steps and shear bands are not as pronounced (Fig. 8d).

The plastic deformation is primarily accommodated in the ultra-fine-grained region (Fig. 8c), which formed after the original cementite grains underwent fragmentation by slip during the first cycles of multi-pass wear. Due to the reciprocating motion and a large number of cycles, the in-plane deformation below the surface is different from the single-pass scratch. The effect of in-plane stresses is particularly evident from the orientation of highly deformed non-cementite particles, which are elongated in the multi-stroke experiment.

In the nanocrystalline region (Fig. 8b), the grains appear equiaxed and nearly spherical, indicating grain rotation and grain boundary sliding. However, the plastic deformation in the nanocrystalline region of the multi-pass scratch is not severe enough to promote the complete decomposition of non-cementite inclusions and their mechanical mixing with cementite. The combined effect of higher wear velocity, lower contact pressure, and presumably higher local temperature is the reason for the slightly larger saturation grain size in the nanocrystalline region and its smaller thickness when compared to the single-pass wear track.

4.3. Strain hardening and softening during sliding wear of cementite

The hardness measurements on the undeformed and worn surfaces provide an estimate of strain hardening during multi-pass wear (Fig. 9a). Please note that the hardness measurements of individual deformed regions in cross-section are not reasonable, as these regions are insufficiently thick to accommodate the complete plastic zone of a nanoindent at a significant depth.

Since the hardness after the wear experiment was dominated by the ultra-fine-grained region, the main possible strengthening mechanisms obstructing dislocation plasticity are grain boundaries (Hall-Petch mechanism) and strain hardening (Taylor hardening). Since indentation was performed outside fractured areas of the worn surface, we presume that deformation mechanisms are still active in the nanocrystalline and ultra-fine-grained regions. Nonetheless, we cannot exclude the influence of cracks on the resulting hardness of the worn areas. We expect grain boundary sliding and grain rotation, associated with strain softening, as the dominant deformation mechanisms in the nanocrystalline and ultra-fine-grained regions. In addition, shear band formation in response to the critical local shear stresses leads to local strain softening. However, shear bands were not observed in the ultra-fine-grained region of the multi-pass wear track (e.g., Fig. 8c).

The interplay of strengthening and softening results in the H_{500nm} increase by 17% (2.7 GPa) compared to the undeformed cementite. Hence, the strengthening effects dominate the softening effects.

4.4. Hägg carbide formation

Hägg carbide (Fe_5C_2 or $Fe_{2.2}C$) is a transition iron carbide that forms during the last tempering stages of the high-carbon martensite and before an equilibrium mixture of iron and cementite is reached [63]. Among the transition carbides that occur during martensite tempering, Hägg carbides are the most stable and can exist in equilibrium with cementite at high carbon concentrations in the shape of microsyntactically intergrown thin layers [64–66]. In the Fischer-Tropsch synthesis, the Hägg carbide is related to the active catalyst phase of the iron-based reaction [67].

This is the first time Hägg carbides were observed after sliding wear experiments on cementite. To explain the formation of Hägg carbide, it is essential to understand the conditions and mechanisms of its precipitation. Several synthesis processes were previously reported. For instance, during the carburization of iron in $CO–H_2–H_2O–H_2S$ gasses at 500 °C for carbon activities exceeding $a_C = 150$ [68], Hägg carbides grow on top of cementite [69]. According to Barinov et al. [70], Hägg carbide formation proceeded after the complete synthesis of cementite during low-temperature ball milling of iron powders in a liquid hydrocarbons medium. The authors argued that the process of less stable high-carbon carbides (i.e., Hägg) transforming into the more stable cementite with less carbon is thus reversible. Another method for Hägg carbide mechanosynthesis involves milling iron and graphite powders in a nitrogen atmosphere [71]. During earlier milling stages, an increase in cementite area fraction was recorded, whereas at extended milling times, the cementite fraction decreased, and Hägg carbide and an ε-carbide fraction increased simultaneously. Higher ball-to-powder ratios and nanoscale refinement accelerated the transformation.

The reported data thus suggests several criteria that induce Hägg carbide formation. Carbon gradients are introduced during the ball milling with carbon-containing components and carburization processes with high carbon activities. The small octahedral interstices in cementite are not favorable for occupation by excess carbon atoms [64] when the stochiometric 25 at.% C concentration is exceeded. Hence, higher carbon concentrations provide a driving force for precipitation. Since the available literature indicates a direct conversion between the two carbides, cementite can be considered a precursor for transformation into the Hägg carbide (and vice versa). Other factors, such as high mechanical energy introduced during mechanosynthesis, nanoscale refinement, and tem-

perature increase during carburization, greatly improve the transformation kinetics. In this work, during the single-pass and multipass sliding wear experiments on cementite, grain refinement, high mechanical energy supplied through friction, wear, and presumably a frictional temperature increase are expected to assist the phase transformation into Hägg carbides. However, the source of the excess carbon in the deformed cementite microstructure is addressed in the following.

We propose two possible sources of excess carbon. One potential source is related to the remaining finely dispersed graphite in the sintered polycrystalline cementite sample (Section 2.1, Fig. 1a). Shearing of the non-cementite particles by a high dislocation activity in a neighboring cementite grain was observed in the transition region of the single-pass wear track (Fig. 4b). In the regions of the highest localized strains, i.e., nanocrystalline region or shear bands, severe shear strains lead to the further decomposition of iron oxide and graphite particles that are subsequently mechanically mixed with the surrounding cementite matrix. In the case of the singlepass wear track, we observe the complete decomposition of noncementite inclusions in the nanocrystalline region (Fig. 3a). In the multi-pass wear track, the decomposition in the nanocrystalline region is limited (Fig. 8b). However, in the area without distinct non-cementite particles of the multi-pass wear track, the diffraction pattern also shows Hägg carbide reflections (Fig. 10).

On the one hand, the thorough mixing of graphite with cementite is expected to increase the overall carbon content in the nanocrystalline region. However, according to APT results (Figs. 6, and A4 in Appendix A), the average carbon content is almost identical in undeformed cementite grain and the nanocrystalline region. The local redistribution of carbon is evident from the 3D sample reconstructions. On the other hand, it is possible that simultaneous mixing of iron oxide and graphite with cementite does not substantially affect the overall iron to carbon ratio, but local carbon enrichment can occur. This explanation is supported by oxygen content increase in APT of the nanocrystalline region and FeO reflections on the diffraction patterns (Figs. 3b, 5b, and 10b).

An alternative source for carbon can arise from oxidation due to tribological loading and frictional heating in the contact zone. The phenomenon of tribo-oxidation was extensively studied in the past and generally occurs in unlubricated steels and alloys [72,73]. Cementite tends to corrode at high temperatures and oxidizes naturally at room temperature, producing amorphous Fe-based oxides and Fe_2O_3 and Fe_3O_4, and other common metallic iron oxides [74]. The carbide oxidation reactions can be accompanied by the formation of CO_2 [75,76], which provides a source of excess carbon for the transformation analogous to the carburization process. Therefore, we suggest that tribo-oxidation can potentially lead to the release of Fe from cementite with Fe forming oxides in the air. Simultaneously carbon enriches the remaining cementite or forms CO_2, both acting as sources for the Hägg carbide formation.

Wear velocity and the associated frictional temperature increase are among the main factors that can accelerate tribo-oxidation. The sliding conditions are not favorable for oxidation in the single-pass wear track since a single stroke at low sliding speed was performed. However, even in these conditions, a slight increase of oxygen content in the nanocrystalline region is observed according to APT results (Fig. 6). This oxygen increase could occur due to the decomposition of the iron oxide FeO particles found in the initial microstructure (Section 2.1, Fig. 1a). Nonetheless, the iron content did not increase similarly in the deformed region. As mentioned above, the constant iron content may be due to the simultaneous decomposition of graphite and iron oxide, leading to the same overall iron to carbon ratio as in the undeformed cementite. However, the most inner reflections of the diffraction pattern from the nanocrystalline region of the single-pass wear track correspond to Fe_2O_3, and Fe_3O_4 oxides (Fig. 5b), which were not detected in the undeformed sample. Therefore, the alternative carbon source based on tribo-oxidation of cementite is also plausible.

When excess carbon is introduced to the microstructure, it is mixed with the surrounding cementite and assisted by microstructure refinement. The deformation-driven cementite fragmentation and high defect density lead to an increase of the free energy associated with the formation of new interfaces [77,78]. This free energy rise leads to increased carbon solubility and allows local supersaturation with carbon atoms. A shift of the XRD peaks from the ultra-fine-grained region to lower angles due to the uniform lattice straining thus is explained by an increase of the carbon content stored within cementite lattice (Fig. 9b). Moreover, the formation of new grain boundaries would further facilitate the redistribution of the excess carbon atoms since the diffusion coefficients at grain boundaries are higher than in bulk [79]. The resulting system would be thermodynamically unstable and can lead to the formation of the Hägg carbide.

The previously proposed mechanisms for enhanced carbon mobility in the pearlitic steel in the vicinity of dislocations are based on the difference between the binding energies of carbon in cementite and carbon at a dislocation core in ferrite [46,80,81]. The binding energy of carbon to dislocations in cementite was not previously investigated. Therefore, these mechanisms are not directly applicable to polycrystalline cementite.

The kinetics of cementite transformation into Hägg carbide is also related to the crystal structure similarities of the two phases. Both structures are often represented by layers of trigonal prisms from iron atoms with carbon atoms located inside the prismatic sites. The individual arrangement of prisms defines the carbide structure and is the basis for the concept of chemical twinning, according to which Hägg carbide can transform into cementite [82,83]. Since the formation of the Hägg carbide occurred solely in the nanocrystalline region with the highest shear strains, we presume that the inverse phase transformation is promoted by straining the carbon-saturated cementite lattice and its subsequent shearing. As a result, a single-pass sliding experiment with high contact pressures is sufficient for the mechanosynthesis of Hägg carbide, as opposed to the previously reported synthesis by ball milling [70,71] that requires a longer duration and long-term diffusion-driven carburization processes [69].

5. Conclusion

We systematically analyzed deformation and chemical evolution in bulk polycrystalline cementite during single-pass and reciprocating multi-pass sliding. We revealed the deformation mechanisms in cementite during wear by means of EBSD and TEM and measured the nanoindentation hardness. The formation of Hägg carbides was reported and further investigated by TEM, XRD, and APT. In summary, the main findings are:

- During sliding wear, cementite deforms plastically through slip activation on (001), (010), (101), (110), and (011) planes. The improved ductility is due to the volume confinement during wear. The stress-strain state due to shear and compression results in moderate plastic deformation and a potential temperature increase in the contact region.
- The cross-sections of single-pass and multi-pass wear tracks reveal gradient deformed microstructures classified into three layers: a top nanocrystalline region, followed by an ultra-fine-grained region, and an extended transition region before the undeformed matrix is reached. Dislocation slip and shear band formation are observed in the transition region, indicating that dislocation-based plasticity is the origin of grain refinement down to 10–20 nm in the nanocrystalline region. We assume that below the contact surface (nanocrystalline region and

ultra-fine-grained region), the highest shear strains are mainly accommodated by grain boundary sliding and grain rotation. These mechanisms lead to the diffraction arcs (preferred orientations) observed in electron diffraction patterns.

- The multi-pass experiment results in the three-body abrasive wear and brittle fatigue crack formation. Outside the fractured regions, the wear track cross-section is characterized by different deformed layers thicknesses compared to single-pass wear. The stress-state is more homogeneous in the transition region of the multi-pass wear track, leading to homogeneously distributed dislocations with no pronounced slip steps or shear band formation. The ultra-fine-grained region is with 4 μm much thicker than in the single-pass wear track with ∼1 μm, whereas the nanocrystalline region has a similar thickness. The interplay of strengthening and softening effects upon deformation results in the nanoindentation hardness increase by up to 17% (2.7 GPa).

- We detect the formation of Hägg carbides in the uppermost nanocrystalline regions of both wear tracks. The nanocrystalline region of the single-passed wear track has locally increased carbon content and a slight but noticeable increase in oxygen. However, the overall carbon content, as well as the carbon to iron ratio, remain similar to the undeformed cementite grain. It is proposed that the excess carbon promotes cementite transformation into Hägg carbide by inducing local carbon enrichment in the cementite phase. This excess carbon may arise due to the deformation-driven decomposition of the finely dispersed graphite particles present in the original microstructure or the tribo-oxidation of cementite, leading to the loss of iron. Other factors, such as high mechanical energy, free energy changes, nanoscale refinement, potential temperature increase, and crystal structure similarities, support the phase transformation.

Declaration of Competing Interest

The authors declare that there are no known conflicts of interest associated with this publication, and there has been no significant financial support for this work that could have influenced its outcome.

Acknowledgments

Supplementary materials

Supplementary material associated with this article can be found, in the online version, at doi:10.1016/j.actamat.2022.117694.

References

[1] G. Langford, Deformation of pearlite, Metall. Trans. A 8 (1977) 861–875.
[2] T. Terashima, Y. Tomota, M. Isaka, T. Suzuki, M. Umemoto, Y. Todaka, Strength and deformation behavior of bulky cementite synthesized by mechanical milling and plasma-sintering, Scr. Mater. 54 (2006) 1925–1929.
[3] Y. Qin, D. Mayweg, P.Y. Tung, R. Pippan, M. Herbig, Mechanism of cementite decomposition in 100Cr6 bearing steels during high pressure torsion, Acta Mater. 201 (2020) 79–93.
[4] X.D. Zhang, A. Godfrey, W. Liu, Q. Liu, Study on dislocation slips in ferrite and deformation of cementite in cold drawn pearlitic steel wires from medium to high strain, Mater. Sci. Technol. 27 (2011) 562–567.
[5] M. Umemoto, Y. Todaka, K. Tsuchiya, Mechanical properties of cementite and fabrication of artificial pearlite, Mater. Sci. Forum 426-432 (2003) 859–864.
[6] N. Argibay, M. Chandross, S. Cheng, J.R. Michael, Linking microstructural evolution and macro-scale friction behavior in metals, J. Mater. Sci. 52 (2017) 2780–2799.
[7] M.W. Kapp, A. Hohenwarter, S. Wurster, B. Yang, R. Pippan, Anisotropic deformation characteristics of an ultrafine- and nanolamellar pearlitic steel, Acta Mater. 106 (2016) 239–248.
[8] J.D. Embury, J.P. Hirth, On dislocation storage and the mechanical response of fine scale microstructures, Acta Metall. Mater. 42 (1994) 2051–2056.
[9] C. Borchers, R. Kirchheim, Cold-drawn pearlitic steel wires, Prog. Mater. Sci. 82 (2016) 405–444.
[10] J. Embury, R. Fisher, The structure and properties of drawn pearlite, Acta Metall. 14 (1966) 147–159.
[11] K. Mishra, A. Pachauri, A. Singh, Deformation, wear and microstructural evolution of nano-structured pearlite under repeated contact sliding, Tribol. Lett. 66 (2018) 365.
[12] B. Narayanaswamy, A. Ghaderi, P. Hodgson, P. Cizek, Q. Chao, M. Safi, H. Beladi, Abrasive wear resistance of ferrous microstructures with similar bulk hardness levels evaluated by a scratch-tester method, Metall. Mat. Trans. A 50 (2019) 4839–4850.
[13] A.J. Perez-Unzueta, J.H. Beynon, Microstructure and wear resistance of pearlitic rail steels, Wear 162-164 (1993) 173–182.
[14] M. Ueda, K. Uchino, T. Senuma, Influence of microstructure on rolling contact wear in high carbon steels, Tetsu Hagane 90 (2004) 1023–1030.
[15] S.D. Bakshi, A. Leiro, B. Prakash, H.K.D.H. Bhadeshia, Dry rolling/sliding wear of nanostructured pearlite, Mater. Sci. Technol. 31 (2015) 1735–1744.
[16] J. Takahashi, M. Kosaka, K. Kawakami, T. Tarui, Change in carbon state by low-temperature aging in heavily drawn pearlitic steel wires, Acta Mater. 60 (2012) 387–395.
[17] Y.J. Li, P. Choi, S. Goto, C. Borchers, D. Raabe, R. Kirchheim, Evolution of strength and microstructure during annealing of heavily cold-drawn 6.3GPa hypereutectoid pearlitic steel wire, Acta Mater. 60 (2012) 4005–4016.
[18] J. Park, S.D. Kim, S.P. Hong, S.I. Baik, D.S. Ko, C.Y. Lee, D.L. Lee, et al., Quantitative measurement of cementite dissociation in drawn pearlitic steel, Mater. Sci. Eng. A 528 (2011) 4947–4952.
[19] F. Wetscher, R. Pippan, S. Sturm, F. Kauffmann, C. Scheu, G. Dehm, TEM investigations of the structural evolution in a pearlitic steel deformed by high-pressure torsion, Metall. Mat. Trans. A 37 (2006) 1963–1968.
[20] S. Djaziri, Y. Li, G.A. Nematollahi, B. Grabowski, S. Goto, C. Kirchlechner, A. Kostka, et al., Deformation-induced martensite: a new paradigm for exceptional steels, Adv. Mater. 28 (2016) 7753–7757.
[21] S.F. Wayne, S.L. Rice, K. Minakawa, H. Nowotny, The role of microstructure in the wear of selected steels, Wear 85 (1983) 93–106.
[22] A.K. Padap, G.P. Chaudhari, S.K. Nath, Mechanical and dry sliding wear behavior of ultrafine-grained AISI 1024 steel processed using multiaxial forging, J. Mater. Sci. 45 (2010) 4837–4845.
[23] R. Ordóñez Olivares, C.I. Garcia, A. DeArdo, S. Kalay, F.C. Robles Hernández, Advanced metallurgical alloy design and thermomechanical processing for rails steels for North American heavy haul use, Wear 271 (2011) 364–373.
[24] Y. Todaka, M. Umemoto, K. Tsuchiya, Microstructural change of cementite in carbon steels by deformation, Mater. Sci. Forum 449-452 (2004) 525–528.
[25] A. Mussi, P. Cordier, S. Ghosh, N. Garvik, B.C. Nzogang, P. Carrez, S. Garruchet, Transmission electron microscopy of dislocations in cementite deformed at high pressure and high temperature, Philos. Mag. 96 (2016) 1773–1789.
[26] H. Ghaffarian, A. Karimi Taheri, K. Kang, S. Ryu, Molecular dynamics simulation study of the effect of temperature and grain size on the deformation behavior of polycrystalline cementite, Scr. Mater. 95 (2015) 23–26.
[27] A. Kumar, G. Agarwal, R. Petrov, S. Goto, J. Sietsma, M. Herbig, Microstructural evolution of white and brown etching layers in pearlitic rail steels, Acta Mater. 171 (2019) 48–64.
[28] H. Chen, C. Zhang, W. Liu, Q. Li, H. Chen, Z. Yang, Y. Weng, Microstructure evolution of a hypereutectoid pearlite steel under rolling-sliding contact loading, Mater. Sci. Eng. A 655 (2016) 50–59.
[29] D. Mayweg, L. Morsdorf, X. Wu, M. Herbig, The role of carbon in the white etching crack phenomenon in bearing steels, Acta Mater. 203 (2021) 116480.
[30] A. Greco, S. Sheng, J. Keller, A. Erdemir, Material wear and fatigue in wind turbine systems, Wear 302 (2013) 1583–1591.
[31] J. Pan, L. Chen, C. Liu, G. Zhang, R. Ren, Relationship between the microstructural evolution and wear behavior of U71Mn rail steel, J. Mater. Eng. Perform. 30 (2021) 1090–1098.
[32] L.E. Karkina, I.N. Karkin, I.G. Kabanova, A.R. Kuznetsov, Crystallographic analysis of slip transfer mechanisms across the ferrite/cementite interface in carbon steels with fine lamellar structure, J. Appl. Crystallogr. 48 (2015) 97–106.
[33] K. Zhang, Z.B. Wang, Strain-induced formation of a gradient nanostructured surface layer on an ultrahigh strength bearing steel, J. Mater. Sci. Technol. 34 (2018) 1676–1684.
[34] M. Umemoto, Z.G. Liu, H. Takaoka, M. Sawakami, K. Tsuchiya, K. Masuyama, Production of bulk cementite and its characterization, Metall. Trans. A 32 (2001) 2127–2131.
[35] B. Zheng, Z. Huang, J. Xing, Y. Wang, Y. Jian, X. Xiao, X. Fan, Three-body abrasive behavior of cementite–iron composite with different cementite volume fractions, Tribol. Lett. 62 (2) (2016) 32.
[36] A.A. Al-Joubori, C. Suryanarayana, Synthesis and thermal stability of homogeneous nanostructured Fe_3C (cementite), J. Mater. Sci. 53 (2018) 7877–7890.

[37] T. Sasaki, T. Yakou, M. Umemoto, Y. Todaka, Two-body abrasive wear property of cementite, Wear 260 (2006) 1090–1095.

[38] H. Tsybenko, F. Farzam, G. Dehm, S. Brinckmann, Scratch hardness at a small scale: experimental methods and correlation to nanoindentation hardness, Tribol. Int. 163 (2021) 107168.

[39] S. Brinckmann, G. Dehm, Nanotribology in austenite: plastic plowing and crack formation, Wear 338-339 (2015) 436–440.

[40] S. Brinckmann, C.A. Fink, G. Dehm, Nanotribology in austenite: normal force dependence, Wear 338-339 (2015) 430–435.

[41] H. Hertz, Über die Berührung fester elastischer Körper, J. Die Reine Angew. Math. 92 (1881) 156–171.

[42] P.J. Schreiber, J. Schneider, Liquid superlubricity obtained for self-mated silicon carbide in nonaqueous low-viscosity fluid, Tribol. Int. 134 (2019) 7–14.

[43] J. Takahashi, K. Kawakami, Y. Kobayashi, Quantitative analysis of carbon content in cementite in steel by atom probe tomography, Ultramicroscopy 111 (2011) 1233–1238.

[44] G. Miyamoto, K. Shinbo, T. Furuhara, Quantitative measurement of carbon content in Fe–C binary alloys by atom probe tomography, Scr. Mater. 67 (2012) 999–1002.

[45] J. Takahashi, K. Kawakami, Y. Kobayashi, Study on quantitative analysis of carbon and nitrogen in stoichiometric θ-Fe$_3$C and γ'-Fe$_4$N by atom probe tomography, Microsc. Microanal. 26 (2020) 185–193.

[46] Y.J. Li, P. Choi, C. Borchers, S. Westerkamp, S. Goto, D. Raabe, R. Kirchheim, Atomic-scale mechanisms of deformation-induced cementite decomposition in pearlite, Acta Mater. 59 (2011) 3965–3977.

[47] B. Gault, M.P. Moody, J.M. Cairney, S.P. Ringer, Atom Probe Microscopy, Springer, New York, New York, NY, 2012.

[48] A. Inoue, T. Ogura, T. Masumoto, Microstructures of deformation and fracture of cementite in pearlitic carbon steels strained at various temperatures, Metall. Mat. Trans. A 8 (1977) 1689–1695.

[49] J. Alkorta, J.G. Sevillano, Assessment of elastic anisotropy and incipient plasticity in Fe$_3$C by nanoindentation, J. Mater. Res. 27 (2012) 45–52.

[50] J. Sevillano, Room temperature plastic deformation of pearlitic cementite, Mater. Sci. Eng. 21 (1975) 221–225.

[51] L.E. Kar'kina, T.A. Zubkova, I.L. Yakovleva, Dislocation structure of cementite in granular pearlite after cold plastic deformation, Phys. Metals Metallogr. 114 (2013) 234–241.

[52] J.S. Lehmann, R. Schwaiger, M. Rinke, C. Greiner, How tribo-oxidation alters the tribological properties of copper and its oxides, Adv. Mater. Interfaces 8 (2021) 2001673.

[53] R.A. Young, The Rietveld method: international workshop papers, Oxford University Press, 1995.

[54] M. Umemoto, Y. Todaka, T. Takahashi, P. Li, R. Tokumiya, K. Tsuchiya, High temperature deformation behavior of bulk cementite produced by mechanical alloying and spark plasma sintering, Mater. Sci. Eng. A 375-377 (2004) 894–898.

[55] D. Tabor, The physical meaning of indentation and scratch hardness, Br. J. Appl. Phys. 7 (1956) 159–166.

[56] M.J. Zehetbauer, H.P. Stüwe, A. Vorhauer, E. Schafler, J. Kohout, The role of hydrostatic pressure in severe plastic deformation, Adv. Eng. Mater. 5 (2003) 330–337.

[57] A. Hohenwarter, A. Taylor, R. Stock, R. Pippan, Effect of large shear deformations on the fracture behavior of a fully pearlitic steel, Metall. Mat. Trans. A 42 (2011) 1609–1618.

[58] G.M. Hamilton, Explicit equations for the stresses beneath a sliding spherical contact, Proc. Inst. Mech. Eng. C J. Mech. Eng. Sci. 197 (1983) 53–59.

[59] J. Takahashi, K. Kawakami, M. Ueda, Atom probe tomography analysis of the white etching layer in a rail track surface, Acta Mater. 58 (2010) 3602–3612.

[60] F.D. Fischer, W. Daves, E.A. Werner, On the temperature in the wheel–rail rolling contact*, Fatigue Fract. Eng. Mater. Struct. 26 (2003) 999–1006.

[61] F. Fang, Y. Zhao, P. Liu, L. Zhou, X. Hu, X. Zhou, Z. Xie, Deformation of cementite in cold drawn pearlitic steel wire, Mater. Sci. Eng. A 608 (2014) 11–15.

[62] A. Bachmaier, R. Pippan, O. Renk, Effect of carbon in severe plastically deformed metals, Adv. Eng. Mater. 22 (2020) 2000879.

[63] M. Dirand, L. Afqir, Identification structurale precise des carbures precipites dans les aciers faiblement allies aux divers stades du revenu, mecanismes de precipitation, Acta Metall. 31 (1983) 1089–1107.

[64] H.K.D.H. Bhadeshia, Theory of Transformations in Steels, CRC Press, Boca Raton, 2021.

[65] G. Ghosh, G.B. Olson, Precipitation of paraequilibrium cementite: experiments, and thermodynamic and kinetic modeling, Acta Mater. 50 (2002) 2099–2119.

[66] Y. Nakamura, T. Mikami, S. Nagakura, In situ high temperature electron microscopic study of the formation and growth of cementite particles at the third stage of tempering of martensitic high carbon steel, Trans. Jpn. Inst. Met. 26 (1985) 876–885.

[67] K. Opeyemi Otun, Y. Yao, X. Liu, D. Hildebrandt, Synthesis, structure, and performance of carbide phases in Fischer-Tropsch synthesis: a critical review, Fuel 296 (2021) 120689.

[68] H.J. Grabke, D. Grassl, H. Schachinger, K.H. Weissohn, J. Wünning, U. Wyss, Methoden zum Messen des Kohlenstoffpegels beim Gasaufkohlen, HTM J. Heat Treat. Mater. 49 (1994) 306–317.

[69] A. Schneider, G. Inden, Carbon diffusion in cementite (Fe$_3$C) and Hägg carbide (Fe$_5$C$_2$), Calphad 31 (2007) 141–147.

[70] V.A. Barinov, A.V. Protasov, V.T. Surikov, Studying mechanosynthesized Hägg carbide (χ-Fe$_5$C$_2$), Phys. Met. Metallogr. 116 (2015) 791–801.

[71] P. Matteazzi, F. Miani, G.L. Caër, Kinetics of cementite mechanosynthesis, Hyperfine Interact. 68 (1992) 173–176.

[72] T. Quinn, J.L. Sullivan, D.M. Rowson, Origins and development of oxidational wear at low ambient temperatures, Wear 94 (1984) 175–191.

[73] F.H. Stott, The role of oxidation in the wear of alloys, Tribol. Int. 31 (1998) 61–71.

[74] H. Yumoto, Y. Nagamine, J. Nagahama, M. Shimotomai, Corrosion and stability of cementite films prepared by electron shower, Vacuum 65 (2002) 527–531.

[75] A.K. Galwey, D.M. Jamieson, B.R. Wheeler, R. Reed, The oxidation of cementite, Corros. Sci. 14 (1974) 527–532.

[76] J. Freel, B.R. Wheeler, A.K. Galwey, Kinetic study of the oxidation of the carbides of iron, Trans. Faraday Soc. 66 (1970) 1015.

[77] J. Languillaume, G. Kapelski, B. Baudelet, Cementite dissolution in heavily cold drawn pearlitic steel wires, Acta Mater. 45 (1997) 1201–1212.

[78] X. Sauvage, J. Copreaux, F. Danoix, D. Blavette, Atomic-scale observation and modelling of cementite dissolution in heavily deformed pearlitic steels, Philos. Mag. A 80 (2000) 781–796.

[79] Y. Ivanisenko, X. Sauvage, I. MacLaren, H.J. Fecht, Nanostructuring and dissolution of cementite in pearlitic steels during severe plastic deformation, in: H. Hahn, A. Sidorenko, I. Tiginyanu (Eds.), Nanoscale Phenomena, Springer, Berlin Heidelberg, Berlin, Heidelberg, 2009, pp. 41–55.

[80] X. Sauvage, Y. Ivanisenko, The role of carbon segregation on nanocrystallisation of pearlitic steels processed by severe plastic deformation, J. Mater. Sci. 42 (2007) 1615–1621.

[81] V.N. Gridnev, V.G. Gavrilyuk, I.Y. Dekhtyar, Y.Y. Meshkov, P.S. Nizin, V.G. Prokopenko, Investigation of carbide phase in strained steel by the method of nuclear gamma resonance, Phys. Status Solidi (a) 14 (1972) 689–694.

[82] G.L. Caer, J.M. Dubois, M. Pijolat, V. Perrichon, P. Bussiere, Characterization by Moessbauer spectroscopy of iron carbides formed by Fischer-Tropsch synthesis, J. Phys. Chem. 86 (1982) 4799–4808.

[83] G. Le CaËr, E. Bauer-Grosse, Aperiodic carbides formed by crystallization of amorphous Fe-C alloys, Hyperfine Interact. 47-48 (1989) 55–67.